



Multiscale label-free imaging of myelin in human brain tissue with polarization-sensitive optical coherence tomography and birefringence microscopy: supplement

NATHAN BLANKE,^{1,†,*}  SHUAIBIN CHANG,^{2,†}  ANNA NOVOSELTSEVA,¹ HUI WANG,³ DAVID A. BOAS,¹ AND IRVING J. BIGIO^{1,2}

¹*Department of Biomedical Engineering, Boston University, 44 Cummington Mall, Boston, MA 02215, USA*

²*Department of Electrical & Computer Engineering, Boston University, 8 St. Mary's St., Boston, MA 02215, USA*

³*Department of Radiology, Athinoula A. Martinos Center for Biomedical Imaging, Massachusetts General Hospital, 149 13th St., Charlestown, MA 02129, USA*

[†]*These authors contributed equally to this work*

*nblanke@bu.edu

This supplement published with Optica Publishing Group on 24 October 2023 by The Authors under the terms of the [Creative Commons Attribution 4.0 License](#) in the format provided by the authors and unedited. Further distribution of this work must maintain attribution to the author(s) and the published article's title, journal citation, and DOI.

Supplement DOI: <https://doi.org/10.6084/m9.figshare.24101427>

Parent Article DOI: <https://doi.org/10.1364/BOE.499354>

1. Supplementary methods for BRM

1.1 BRM instrumentation

Our custom BRM setup (Fig. 3) is a revised design from [1] that provides increased efficiency and throughput. The BRM system uses a high-power red ($\lambda = 625$ nm) LED for illumination (Thorlabs M625L4), paired with corresponding polarization optics in collimated (infinity) space of the illumination and detection arms of the microscope. The polarization optics consist of a linear polarizer (Thorlabs LPVISE100-A) and a QWP (Thorlabs WPQ10ME-633) in each arm, with each optical element mounted on a high-speed rotation stage (Thorlabs ELL14). High-speed stages enable precision scanning of the sample in XY (Thorlabs MLS203-1) and the objective in Z (Thorlabs ZFM2020). Imaging is performed with a range of air objectives from 4X to 40X magnification (Olympus UPLFLN4X, UPLFLN10XP, UPLFLN20XP, UPLNFLN40XP) or a 60X oil-immersion objective (Olympus UPLSAPO60XO). To maximize volumetric imaging throughput, our BRM system utilizes a high density sCMOS camera (Teledyne Iris 9).

For CCP-BRM, imaging is performed between circular polarizer and analyzer of opposite handedness, which are set up by rotating the illumination-side and detection-side linear polarizers to 45° and -45° to the fast axes of their respective QWPs. For optimum extinction ratio, the circular polarizer and circular analyzer should be oriented such that their linear polarizers are crossed. For qBRM, the detection-side optics (circular analyzer) remain the same, but for illumination with linearly polarized light, the illumination polarizer is synchronized to be parallel with the fast (or slow) axis of its QWP, and both are then rotated in tandem to maintain linearly polarized illumination, with multiple incident polarization angles. With independent control over the rotational settings of the linear polarizers and QWPs, our BRM system design conveniently enables both rapid acquisition of qBRM images and efficient toggling between the CCP-BRM and qBRM imaging modalities.

1.2 qBRM image analysis and visualization

During qBRM, the sample is illuminated with a sequence of linear polarization states, and the resulting sinusoidal signal, Eq. (5), is analyzed for each pixel in the image to extract the amplitude, phase, and DC-offset, which correspond to the relative retardance, $|\sin(2\pi\delta)|$, in-plane optic-axis orientation, ϕ , and transmittance, I_0 , respectively. For each qBRM image set, images are taken of the sample at evenly spaced polarizer rotation angles of 0° , 60° and 120° , resulting in unprocessed qBRM images with intensities, $I_{sample}(\theta)$. A corresponding set of unprocessed qBRM images are taken in an empty region of the sample plane to measure the intensity changes due to residual system birefringence, $I_{system}(\theta)$. With this optical setup, the predominant source of system birefringence is from the use of a monochromatic QWP (in the circular analyzer) with a narrow but finite bandwidth LED for illumination. (For non-center wavelengths of the LED, the circular analyzer transmits elliptically polarized light with a preferential axis.) To correct each qBRM image set, the oscillatory component of the system birefringence measurement is subtracted from the sample birefringence measurement:

$$I_{corr}(\theta) = I_{sample}(\theta) - [I_{system}(\theta) - \text{mean}(I_{system}(\theta))]. \quad (S1)$$

Following subtraction of system birefringence, the corrected images, $I_{corr}(\theta)$, can be analyzed directly to determine birefringence parameters, with parallel processing for all pixels across the entire image. For the specific polarizer rotation angles of 0° , 60° and 120° , which are evenly spaced over the range of orientations (0° to 180°) for birefringence data, Eq. (5) can be solved (with MATLAB symbolic variables) for each of the three birefringence parameters, where $I_1 = I_{corr}(0^\circ)$, $I_2 = I_{corr}(60^\circ)$ and $I_3 = I_{corr}(120^\circ)$:

$$|\sin(2\pi\delta)| = \frac{2\sqrt{I_1^2 + I_2^2 + I_3^2 - I_1I_2 - I_1I_3 - I_2I_3}}{I_1 + I_2 + I_3} \quad (S2)$$

$$\varphi = \tan^{-1} \left(\frac{I_2\sqrt{3} - I_3\sqrt{3} + 2\sqrt{I_1^2 + I_2^2 + I_3^2 - I_1I_2 - I_1I_3 - I_2I_3}}{-2 \cdot I_1 + I_2 + I_3} \right) \quad (\text{S3})$$

$$I_0 = \frac{2}{3}(I_1 + I_2 + I_3). \quad (\text{S4})$$

The two birefringence parameter maps are the relative retardance [Eq. (S2)] and the in-plane optic-axis orientation [Eq. (S3)]. The transmittance [Eq. (S4)] map, on the other hand, describes the loss of unpolarized light during transmission through the thin section, which can be assumed to be entirely due to scattering (given negligible absorption at this wavelength) in fixed brain tissue. We typically do not analyze the transmittance map for high-resolution imaging of myelin, but by decoupling the transmittance effects from the qBRM measurement, myelin anisotropy can be quantified with high sensitivity and contrast. We note that the values of $|\sin(2\pi\delta)|$, φ and I_0 can be extracted from Eq. (5) by fitting a sine function to the measured intensities at multiple (typically 6+) illumination-polarizer angles, θ [2,3]; however, the solution to the three equations above is computationally more efficient and equally accurate.

For visualization of the qBRM parameter maps, the relative retardance, $|\sin(2\pi\delta)|$, can be displayed as a grayscale intensity image or as a “heat map,” and the angular optic-axis orientation map, φ , is converted into a color-coded optic-axis orientation map based on a color-wheel. In the color orientation images, the intensity of each pixel is then assigned based on the relative retardance map, producing the final retardance-weighted optic-axis orientation map. Retardance weighting provides shading to the color orientation image and effectively masks out pixels that are not birefringent. Retardance-weighted optic-axis orientation maps provide detailed images of myelin anisotropy, with both birefringence parameters combined into a single image.

Lastly, all qBRM parameter maps required stitching of multiple tiles into a final image, with the stitching pipeline dependent on the scale of imaging during acquisition and on the area imaged. For the low-resolution (10X) qBRM images of the entire tissue section, single-plane qBRM images were acquired and analyzed at each tile location, and then birefringence parameter maps were stitched in Fiji [4]. For the higher-resolution (20X) qBRM images, qBRM z-stacks were acquired and analyzed at each tile location; but, before stitching the birefringence parameter maps in Fiji, the high-resolution z-stacks were focus-stacked with Adobe Photoshop. Focus stacking is an image processing technique that synthesizes an in-focus image from multiple planes of a z-stack to artificially increase the depth of field [5–7]. In focus-stacked qBRM images, resolved individual myelinated axons are displayed in their entirety, along the full thickness of the section, whereas they may otherwise dip in- and out-of-focus within a single-plane image. This approach, of the stitching of high-resolution focus stacks, is significantly less computationally intensive than a scheme wherein volumetric images are stitched together, albeit at the expense of losing some volumetric information across each z-stack.

1.3 qBRM optic-axis orientation artifacts introduced by scattering

Within this paper, a notable feature of the high-resolution qBRM optic-axis orientation maps is that scattering structures [e.g., the yellow-colored air bubble indicated by the yellow arrow in Fig. 7(b)] have the “system” birefringence and its corresponding orientation from the color-wheel applied to them. During the qBRM measurement, while rotating a linear polarizer against a circular analyzer, structures with a low transmittance (high scattering) are darker than the DC-level, and as a result of the correction for system birefringence that is employed, these scattering structures are assigned an artifactual “orientation” (color) based on the system-correction value. This artifact from scattering can also be seen within the through-plane blood vessel of Fig. 7(c) and within many locations of the brightness-enhanced image of Layer I/II of the cortex [Fig. 7(d)], where non-birefringent scatterers are given a yellow color. This effect for scattering structures can be computationally removed or labeled in a different manner (i.e., shaded black or white) with a transmittance-weighting approach, but it was not performed on the qBRM optic-axis orientation maps presented here. A potential benefit of this imaging “artifact” is that non-birefringent scattering structures are added to the birefringence map for visualization, but labeled so as to avoid confusing the two, providing an additional contrast mechanism and increased information content to the images.

References

1. N. Blanke, V. Go, D. L. Rosene, and I. J. Bigio, "Quantitative birefringence microscopy for imaging the structural integrity of CNS myelin following circumscribed cortical injury in the rhesus monkey," *Neurophotonics* **8**, 1–15 (2021).
2. M. Axer, K. Amunts, D. Grässel, C. Palm, J. Dammers, H. Axer, U. Pietrzyk, and K. Zilles, "A novel approach to the human connectome: Ultra-high resolution mapping of fiber tracts in the brain," *Neuroimage* **54**, 1091–1101 (2011).
3. A. M. Glazer, J. G. Lewis, and W. Kaminsky, "An automatic optical imaging system for birefringent media," *Proc. R. Soc. Ser. A Math. Phys. Eng. Sci.* **452**, 2751–2765 (1996).
4. S. Preibisch, S. Saalfeld, and P. Tomancak, "Globally optimal stitching of tiled 3D microscopic image acquisitions," *Bioinformatics* **25**, 1463–1465 (2009).
5. B. Forster, D. Van De Ville, J. Berent, D. Sage, and M. Unser, "Complex wavelets for extended depth-of-field: A new method for the fusion of multichannel microscopy images," *Microsc. Res. Tech.* **65**, 33–42 (2004).
6. L. Chen and S. Zhang, "Large depth-of-field microscopic structured-light 3D imaging with focus stacking," *Opt. Lasers Eng.* **167**, 107623 (2023).
7. S. Pertuz, D. Puig, M. A. Garcia, and A. Fusiello, "Generation of All-in-Focus Images by Noise-Robust Selective Fusion of Limited Depth-of-Field Images," *IEEE Trans. Image Process.* **22**, 1242–1251 (2013).